

# Effect of Flow Rate Controllers and their Opening Levels on Liquid Steel Flow in Continuous Casting Mold

Kadir Ali GURSOY and Mehmet Metin YAVUZ\*

Department of Mechanical Engineering, Middle East Technical University, Dumlupınar Blv. No: 1, 06800 Çankaya Ankara, Turkey.

(Received on September 5, 2015; accepted on December 17, 2015)

The present study investigates the mold flow structure at constant throughput condition for different slide-gate and stopper rod openings by utilizing computational fluid dynamic (CFD) modeling. Detailed validation of the CFD models are conducted using available experimental data and the performances of three different turbulence models, standard  $k-\varepsilon$ , realizable  $k-\varepsilon$  and  $k-\omega$  SST are compared. The constant throughput casting operations for different slide-gate and stopper rod controller openings are simulated to quantify the effect of flow controllers and their opening levels on mold flow. The results indicate that for a slide-gate controlled system, the meniscus velocities are significantly affected by the changes in the opening level. The steady state operations do not provide the same mold flow if the slide-gate opening is altered. However, for the stopper rod controlled system the stopper rod opening level changes do not affect the meniscus velocities and the flow structures within the mold.

KEY WORDS: mold flow; continuous casting; CFD, turbulence modeling; flow controller; slide-gate; stopper rod.

## 1. Introduction

Continuous casting system is known to be operating most efficiently under the steady state conditions.<sup>1)</sup> Transport rate of molten steel from tundish to the caster mold is among the parameters desired to be constant. In continuous casting operation of steel, the flow through tundish to the mold can be controlled by different flow rate control systems including stopper rod and slide-gate.<sup>2)</sup> These two tundish flow rate control mechanisms are commonly preferred in industry, where each one has its own advantages and shortcomings.<sup>3)</sup> Ladle changes in continuous casting machines result in liquid steel level changes in tundishes. During this transient event of production, the flow rate controller opening is increased to reduce the pressure drop across the opening which helps to keep the mass flow rate at the desired level for the reduced liquid steel level in tundish.

Extensive and elaborate past work were conducted on the different aspects of tundish flow controllers of continuous casting machine such as slide-gate opening fraction, slide-gate orientation, slide-gate design, stopper rod movement, stopper rod tilt and stopper rod misalignment, stopper rod sticking and the influence of these parameters on the mold flow structure.<sup>4-12)</sup> However, they all focus on one type of controller, therefore in literature there is no complete study focusing on the influence of flow controller type on mold flow structure.

This work presents a unique comparison of the two

flow controller types; slide-gate and stopper rod, and provides information for their performance under the constant throughput condition. In addition, based on the results of the conducted simulations, the study suggests alterations in some of the common practices of continuous casting for producing the same quality steel through the casting process.

Bai H. and Thomas B.G. worked on their slide-gate controlled geometry.<sup>4,5)</sup> The flow within the domain was multi-phase with the presence of argon gas. The analyses were conducted using multifluid Eulerian multiphase model built in ANSYS CFX<sup>TM-16)</sup>, later the results were verified using experimentation data and then they investigated the influence slide-gate opening fraction and slide-gate orientation.<sup>5)</sup> Kononov *et al.*<sup>6)</sup> designed new slide-gate systems for ingot and shaped castings. Chaudhary *et al.*<sup>7)</sup> studied on the three stopper rod placements, aligned, front-misaligned and left-misaligned and observed the influence of the resulting asymmetric flow due to misaligned stopper rods. Liu *et al.*<sup>8)</sup> developed a mathematical model to quantify the flow rate history through the submerged entry nozzle (SEN) due to stopper rod movement and compared with the plant measurements.<sup>8)</sup> Lima *et al.* investigated the mechanisms behind the stopper rod sticking and proposed solution for preventing the problem.<sup>9)</sup>

This paper aims to investigate the effect of different flow controllers on mold flow structure using Computational Fluid Dynamics (CFD) modeling. For this purpose, first the simulation domain is constructed and a mesh independency study is performed. Then the performance of three different turbulence models is evaluated and the models are validated against the water model test results. Based on this evalua-

\* Corresponding author: E-mail: ymetin@metu.edu.tr  
DOI: <http://dx.doi.org/10.2355/isijinternational.ISIJINT-2015-440>

tion, a suitable turbulence model is selected to be used for the rest of the present study. Finally, to quantify the effect of flow controller type and their opening ratios on mold flow structure, the stopper rod and slide-gate controlled domains are simulated and compared at different opening levels. For the validation study, the water model results are extracted from a previous work which utilizes a Particle Image Velocimetry (PIV) system for velocity measurements. PIV is a non-intrusive planar measurement method which can provide the instantaneous global velocity field.<sup>13,14</sup> PIV system uses pulsed laser sheet to illuminate the flow field of interest which contains tracer particles and the position of the particles are recorded with a digital camera system for the each pulse of the laser. Since the particle displacements are calculated using statistical correlation and the time interval between the each pulse is known, corresponding velocity vectors can be computed.<sup>13,14</sup> The water model results are taken from the work of Thomas *et al.*<sup>15</sup> where a standard PIV system provides two velocity components in a plane of interest. The mentioned study provides velocity information at several locations including the exit plane of the SEN, along the jet direction, and at the meniscus region.

## 2. Model Development and Mesh Independency Study

The CFD model was developed for 0.4-scale water model which includes the nozzle and the mold as shown in Fig. 1.<sup>15</sup> The geometry was created using ANSYS Design Modeler<sup>TM-16</sup>. The particular geometry was selected since the

geometry contains sufficient experimental data which was used to validate the CFD model developed in the present study.<sup>15</sup> The details of the geometry along with the corresponding boundary conditions are tabulated in Table 1. Flow control was provided by a slide-gate mechanism. The slide-gate opening is 40%, area fraction. The fixed flow rate was supplied from the inlet of the UTN (Upper Tundish Nozzle). Three 35 mm square openings at the bottom surface were the outlet ports. The top surface, meniscus region, was modeled as free slip boundary condition where the flow was free of any shear stresses to simulate the condition for water model test set-up. The side walls including SEN walls were modeled as no slip boundary condition where the fluid had zero velocity relative to the adjacent walls. When the only half of the domain was simulated, the symmetry boundary condition was utilized. The image on the left of Fig. 1(a) demonstrates the simulation domain along with the corresponding boundary conditions for half domain simulations. The images on the right side of the Fig. 1(a) demonstrate the zoomed in representation for the slide-gate section in the simulation domain along with the stopper rod section that is used in further sections where the effect of different types of flow rate controllers on mold flow is investigated.

In the present study ANSYS Meshing<sup>TM-16</sup> was used for grid generation and ANSYS FLUENT<sup>TM-16</sup> was utilized for performing the flow simulations. The unstructured grid for the whole domain consisted of 3D tetrahedral elements and prismatic inflation layers. Patch conforming method was utilized for the creation of the mesh. The mesh was designed to get finer on the certain areas which were anticipated to have the greatest velocity gradients such as slide-gate and port sections. Lower in the mold region mesh elements start to grow. The boundary layer was created using inflation option available within in the Meshing. The details of the meshes used in the mesh independency study are tabulated in Table 2. The mesh independency study was only performed for the slide-gate controlled geometry, for the stopper rod controlled geometries similar mesh size controllers were utilized. Samples from the slices of the mesh at slide-gate, SEN inlet and stopper rod inlet regions along the symmetry plane are illustrated in Fig. 1(b).

The mesh independency study was performed to make

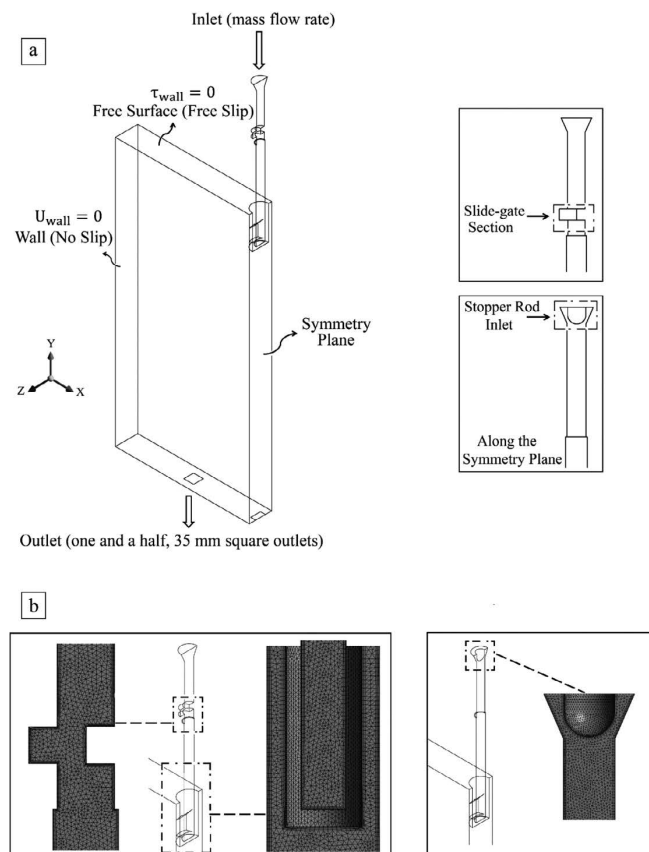


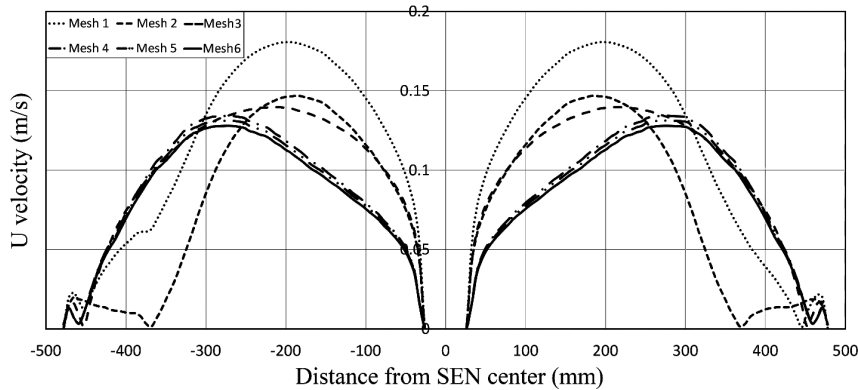
Fig. 1. (a) Typical simulation domain and boundary conditions used in CFD models, (b) slices of the mesh parallel to the side wall at slide gate, SEN, and stopper rod inlet, respectively.

Table 1. Dimensions and boundary conditions of the model.

Flow rate	0.70 kg/s	Liquid Density	998.2 kg/m <sup>3</sup>
Total nozzle length	510 mm	SEN submergence depth	80 mm
Slide-gate opening, $f_A$	40%	Slide-gate orientation	90°
Slide-gate thickness	18 mm	Slide-gate diameter	28 mm
Nozzle bore diameter	32 mm	UTN diameter	28 mm
Port opening	31×31 mm	Port thickness	11 mm
Port upper angle	40°	Port lower angle	15°
Mold length	956 mm	Mold thickness	80 mm
Side walls	No slip	Top surface	Free slip
Inlet	Mass flow rate	Outlet	Pressure outlet

**Table 2.** Mesh parameters used in the mesh independence study.

Algorithm	Tetrahedrons and Prismatic Elements					
Method	Patch Conforming					
	Mesh 1	Mesh 2	Mesh 3	Mesh 4	Mesh 5	Mesh 6
Nodes	391 724	796 612	900 852	1 059 852	1 385 712	1 972 591
Elements	1 030 945	2 439 675	3 101 733	4 023 953	5 114 789	8 887 628
Maximum Skewness	0.90	0.89	0.89	0.88	0.87	0.87
Minimum Orthogonal Quality	0.14	0.15	0.15	0.17	0.17	0.18

**Fig. 2.** Meniscus velocities at the center plane of the mold parallel to the broad face for six different meshes.

sure the solutions were independent of mesh density. The element number was increased until the solution did not change more than 1%. The standard  $k$ - $\epsilon$  turbulence model was used along with the enhanced wall treatment option, for the mesh independency study. Second order upwind discretization scheme was utilized for spatial discretization of the momentum, turbulent kinetic energy and the turbulent dissipation rate. Second order upwind method was selected because it is known to yield more accurate results than the first order upwind scheme for tetrahedral grids. Semi-Implicit Method for Pressure Linked Equations<sup>16)</sup> (SIMPLE) algorithm was the chosen pressure-velocity coupling scheme as it is known to be an efficient method for steady state analyses.<sup>16)</sup>

A typical simulation of whole domain took approximately 13 hours of computing time. The residual values of the velocity components are plotted to check the convergence behavior. The ultimate degree of convergence of the solutions were determined by the monitor points located on several locations within the mold. The velocity magnitudes on the monitor points were plotted and the convergence of the solutions were decided on their trend to change.

In order to reach a mesh independent solution, the grid was refined at each time, and six different mesh topologies were constructed. The coarsest mesh has 391 724 nodes and 1 030 945 elements whereas the finest mesh consists of 1 972 591 nodes and 8 887 628 elements. For a comprehensive comparison, **Fig. 2** is constructed for  $u$  component of velocity along the meniscus region at the centerline of the narrow face parallel to the broad face of the mold. The figure demonstrates the absolute values of  $u$  components of velocities. The results indicate that velocity values differ up to 28% between meshes 1 and 3. The velocity trends also show a dramatic change in the results of the corresponding meshes. Starting from Mesh 4 however, the velocity magnitudes do not vary more than 1%. Moreover, **Fig. 2** demonstrates that

the flow fields are symmetrical within the simulation domain.

Further comparisons of the results corresponding to different mesh densities are shown in **Fig. 3** where the velocity magnitudes are plotted at three different locations of the port exit. The sketch on the right hand side of the figure presents the locations of the data lines along which the velocity magnitudes are obtained. The plotted velocities are at the center plane and 6 and 12 mm away from the center plane. The velocity magnitudes were calculated by using the  $u$  and  $v$  components of the velocity only (which are the directions parallel to the broad and narrow faces of the mold respectively, as demonstrated with the coordinate axis shown **Fig. 1**), as the experimental data provided. The results demonstrate that the velocity magnitudes and the general trends show great variations within the range of 6 mm. This is directly linked with the existence of strong circulation in the port exit arising from the slide-gate impact on the flow structure. **Figure 3** demonstrates consistent results with the results indicated in **Fig. 2**. As can be seen in the **Fig. 3** the velocities show great variations between meshes 1–3 raising up to 25%. The predictions of the meshes 4 to 6 are almost identical such that the results do not show variations more than 1%. Considering these results it can be concluded that a mesh independent solution is achieved starting from the mesh 4. Therefore, Mesh 4 emerges as the selected mesh for this study as it contains the least nodes and element numbers among the meshes 4 to 6.

### 3. Turbulence Modeling

The flow in the mold of continuous casting machines is highly turbulent. In order to model this turbulent flow, a suitable turbulence model needs to be identified. Fluent offers different turbulence models varying from simple to highly complex in regard to the modeling part of turbulence nature of the flow. In this study, based on the studies in lit-

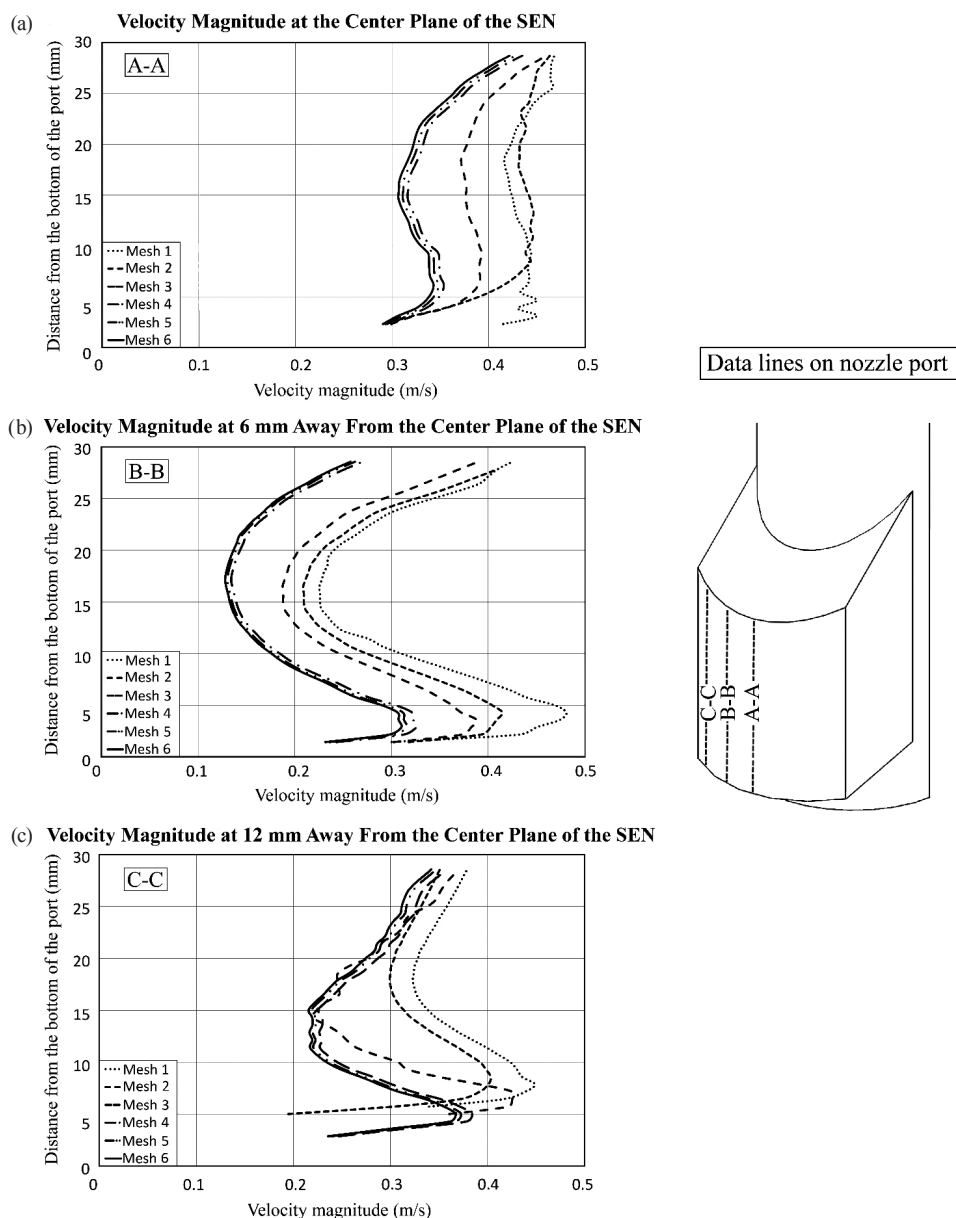


Fig. 3. Velocity values for six different meshes on the lines (a) A-A, center of the port exit, (b) B-B, 6 mm away from center of the port exit, (c) C-C, 12 mm away from center of the port exit.

erature, the performance of three different turbulence models were evaluated and compared to the water model test results. The selected turbulence models were standard  $k-\epsilon$ , realizable  $k-\epsilon$  and  $k-\omega$  Shear Stress Transport (SST) models, where letters  $k$ ,  $\epsilon$ ,  $\omega$  denote turbulent kinetic energy, turbulent dissipation and specific rate of dissipation of the turbulence kinetic energy respectively. For the  $k-\omega$  SST model the mesh was modified in order to keep  $y^+$  value under 1. The first layer thickness in the inflation layer was decreased and quick simulations were performed to determine the current  $y^+$  value. Once the required  $y^+$  value is obtained the final simulations were performed. For all three models, the following Mass Conservation Equation and the Momentum Conservation Equation were solved.<sup>16)</sup>

$$\frac{\partial \rho}{\partial t} + \nabla \cdot (\rho \vec{v}) = 0 \dots\dots\dots (1)$$

$$\frac{\partial}{\partial t} (\rho \vec{v}) + \vec{v} \cdot \nabla (\rho \vec{v}) = -\nabla p + \nabla \cdot (\vec{\tau}) + \rho \vec{g} \dots\dots\dots (2)$$

In the equations above  $\rho$ ,  $t$ ,  $v$ ,  $\tau$ ,  $p$ ,  $g$  stands for density, time, velocity, stress tensor, pressure, gravitational acceleration respectively and  $\nabla$  is the del operator. Other equations solved within each turbulence model are provided below.

For Standard  $k-\epsilon$  Model the turbulence kinetic energy,  $k$ , and its rate of dissipation,  $\epsilon$ , are obtained from the following transport equations;

$$\frac{\partial}{\partial t} (\rho k) + \frac{\partial}{\partial x_i} (\rho k u_i) = \frac{\partial}{\partial x_j} \left[ \left( \mu + \frac{\mu_t}{\sigma_k} \right) \frac{\partial k}{\partial x_j} \right] \dots\dots (3) + G_k + G_b - \rho \epsilon - Y_M + S_k$$

$$\frac{\partial}{\partial t} (\rho \epsilon) + \frac{\partial}{\partial x_i} (\rho \epsilon u_i) = \frac{\partial}{\partial x_j} \left[ \left( \mu + \frac{\mu_t}{\sigma_\epsilon} \right) \frac{\partial \epsilon}{\partial x_j} \right] \dots\dots (4) + C_{1\epsilon} \frac{\epsilon}{k} (G_k + C_{3\epsilon} G_b) - C_{2\epsilon} \rho \frac{\epsilon^2}{k} + S_\epsilon$$

Similarly, Realizable  $k-\epsilon$  Model solves the following transport equations in order to obtain the turbulence kinetic

energy,  $k$ , and its rate of dissipation,  $\varepsilon$ ,

$$\frac{\partial}{\partial t}(\rho k) + \frac{\partial}{\partial x_j}(\rho k u_j) = \frac{\partial}{\partial x_j} \left[ \left( \mu + \frac{\mu_t}{\sigma_k} \right) \frac{\partial k}{\partial x_j} \right] + G_k + G_b - \rho \varepsilon - Y_M + S_k \quad \dots (5)$$

$$\frac{\partial}{\partial t}(\rho \varepsilon) + \frac{\partial}{\partial x_j}(\rho \varepsilon u_j) = \frac{\partial}{\partial x_j} \left[ \left( \mu + \frac{\mu_t}{\sigma_\varepsilon} \right) \frac{\partial \varepsilon}{\partial x_j} \right] + \rho C_{1\varepsilon} S_\varepsilon - C_{2\varepsilon} \rho \frac{\varepsilon^2}{k + \sqrt{g\varepsilon}} + C_{1\varepsilon} \frac{\varepsilon}{k} G_{3\varepsilon} G_b + S_\varepsilon \quad \dots (6)$$

In above equations,  $G_k$ ,  $G_b$  demonstrate the generated turbulent kinetic energy due to the mean velocity gradient and buoyancy respectively. The turbulent viscosity is shown as,  $\mu_t$ .  $C_{1\varepsilon}$ ,  $C_{2\varepsilon}$ ,  $C_{3\varepsilon}$  are constants and  $S_k$ ,  $S_\varepsilon$  are user-defined source terms.  $Y_M$  points out the contribution of the fluctuating dilatation in compressible turbulence to the overall dissipation rate and finally  $\sigma_\varepsilon$ ,  $\sigma_k$  are turbulent Prandtl numbers for  $\varepsilon$  and  $k$  respectively.

The shear-stress transport (SST)  $k-\omega$  Model the turbulence kinetic energy,  $k$ , and specific rate of dissipation,  $\omega$ , are obtained from the following transport equations;

$$\frac{\partial}{\partial t}(\rho k) + \frac{\partial}{\partial x_i}(\rho k u_i) = \frac{\partial}{\partial x_j} \left[ \Gamma_w \frac{\partial k}{\partial x_j} \right] + \widehat{G}_k - Y_k + S_k \dots (7)$$

$$\frac{\partial}{\partial t}(\rho w) + \frac{\partial}{\partial x_i}(\rho w u_i) = \frac{\partial}{\partial x_j} \left[ \Gamma_w \frac{\partial w}{\partial x_j} \right] + G_w - Y_w + D_w + S_w \quad \dots (8)$$

In above equations,  $\widehat{G}_k$  demonstrates the generated turbulent kinetic energy due to the mean velocity gradient.  $\Gamma_w$ ,  $\Gamma_k$  represent the turbulent diffusivity of  $w$  and  $k$  respectively and  $Y_w$ ,  $Y_k$  point out the dissipation of  $w$  and  $k$  due to turbulence.  $S_k$ ,  $S_w$  are used-defined source terms,  $D_w$  is the cross-diffusion term and  $G_w$  show the generation of  $w$ .

The above equations are just a brief summary of the turbulence models, the detail of the formulations can be found elsewhere.<sup>16)</sup>

#### 4. Performance Evaluation of Different Turbulence Models

Upon deciding on the turbulence model the simulations were performed and their results are presented and compared against experimental results. Utilizing the symmetry in the domain only the half of the geometry was simulated in order to reduce the computation time. The normalized velocity vectors for three different turbulence models are plotted at the center plane, parallel to the wide face of the mold as shown in Fig. 4. In constructing the Fig. 4, the lengths of vectors are normalized and thus do not contain velocity magnitude information whereas the greyscale indicates the magnitude of the velocity vectors shown on the left side of the figure. The figure indicates that all three turbulent models succeeded in obtaining the double roll flow pattern within the mold. The strong upper circulation regions are apparent, particularly for the  $k-\varepsilon$  based models. The velocity magnitudes show that the standard and realizable  $k-\varepsilon$  models

predict strong upper circulation with weak lower circulation, whereas, SST model predicts strong lower circulation with weak upper circulation.

The velocity magnitudes in the meniscus region are plotted at the center plane of the narrow face parallel to the broad face of the mold, as demonstrated in Fig. 5. The figure demonstrates that meniscus velocity predictions differ in each turbulence model in terms of both magnitude and trend. The realizable  $k-\varepsilon$  model prediction has the greatest velocity magnitudes whereas the  $k-\omega$  SST model has the lowest.

In order to further distinguish the differences of the results, the velocity magnitudes are plotted at three locations of the port exit in Fig. 6. Figure 6 was constructed using the same approach in Fig. 3 and the schematic illustration of port exit surface is provided on the right side of the figure. Figure 6 provides the velocity magnitude predictions of three turbulence models along with the experimental data from the literature<sup>15</sup>. The PIV results of the experiments are presented at both center and 12 mm away from the center planes<sup>15</sup>. It is important to mention that finite thickness of the laser sheet in PIV experiments varies approximately from 1 to 5 mm, which also determines the resolution of the experiment. It should be noted that the PIV results were obtained by taking the average of the velocity magnitudes within the thickness of the PIV laser. Figure 6 demonstrates that the velocity predictions of turbulence models display great shifts within a distance of 12 mm. In the first 6 mm they experience a velocity decrease up to 45% in average. However, later in the second 6 mm they perform a velocity increase up to 50% in average. The possible mechanisms responsible for these variations are discussed previously in the mesh independency chapter. These velocity shifts support the fact that the resolution of the CFD

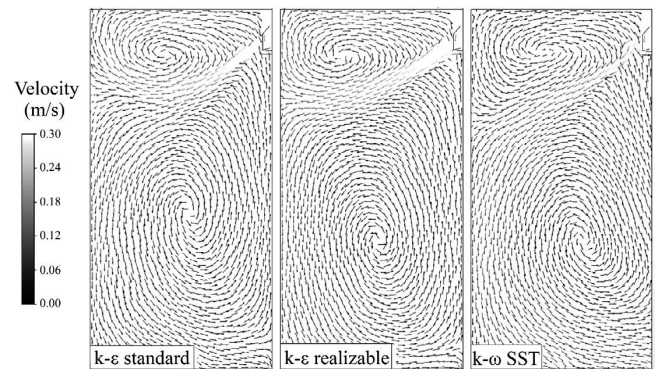


Fig. 4. Normalized velocity vectors at the center plane of the mold for three different turbulence models.

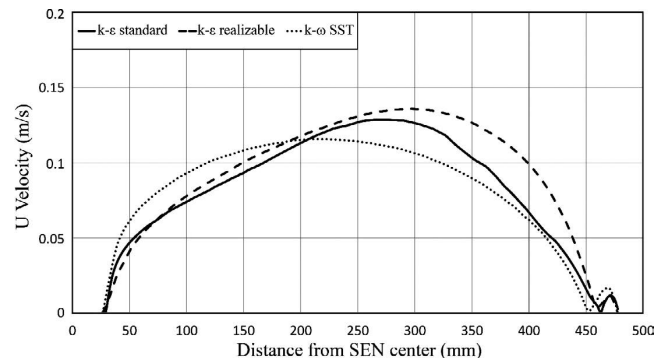


Fig. 5. Meniscus velocities at the center plane of the mold for three different turbulence models.

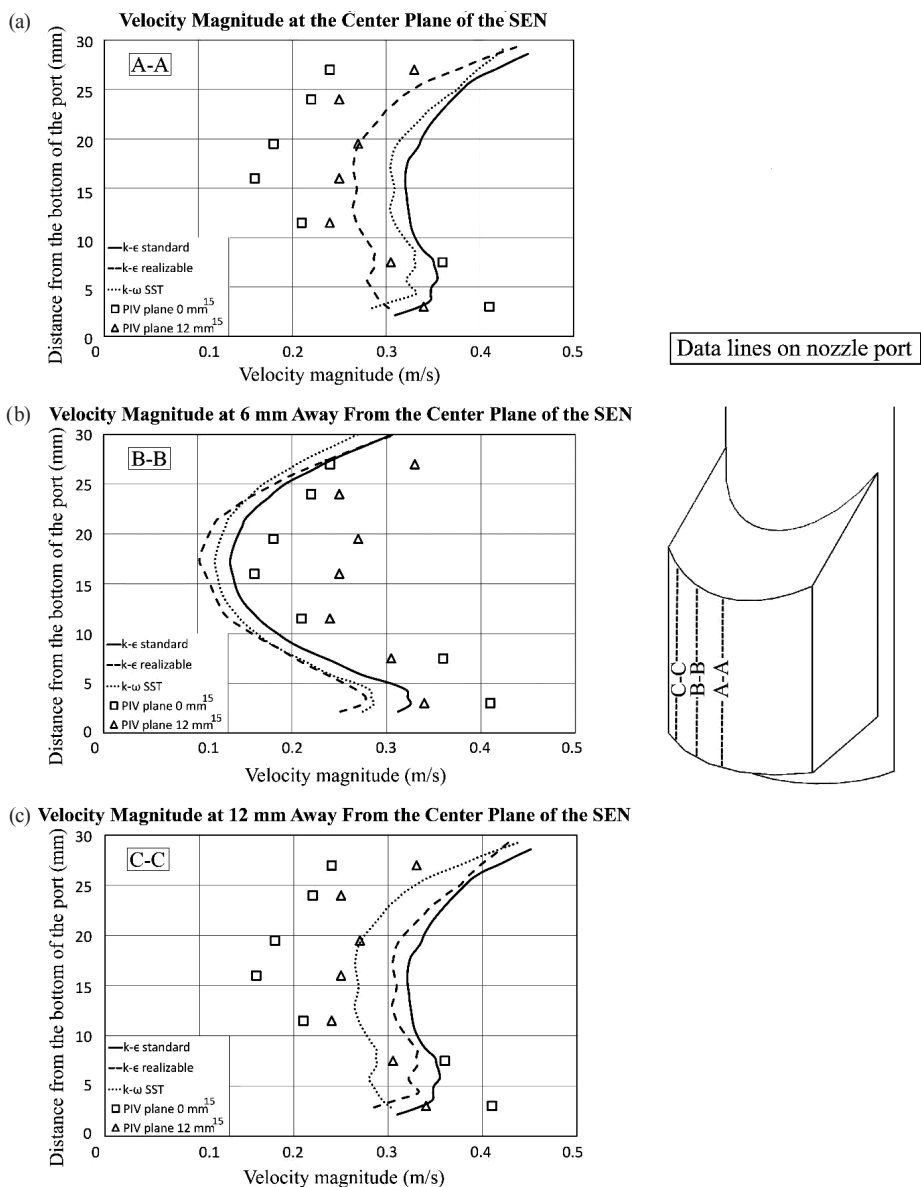


Fig. 6. Velocity values for different turbulence models on the lines (a) A-A, center of the port exit, (b) B-B, 6 mm away from center of the port exit, (c) C-C, 12 mm away from center of the port exit.

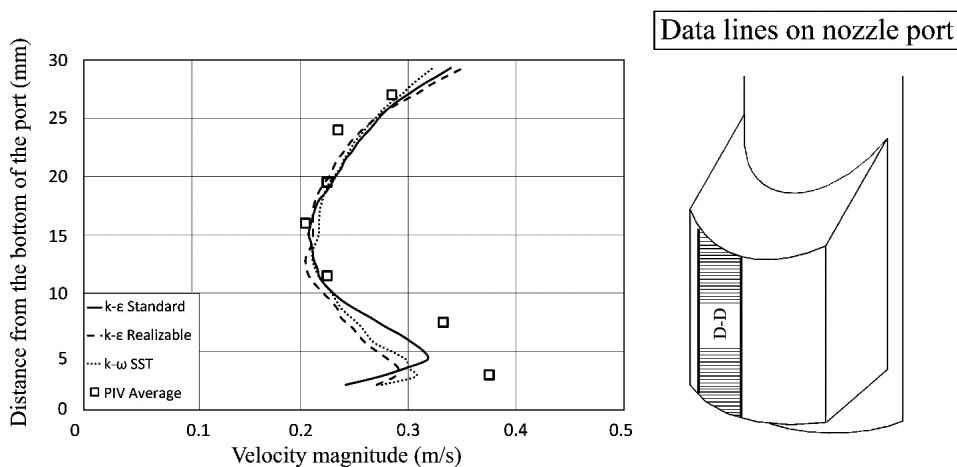


Fig. 7. Average velocity values in region D-D for three turbulence models and PIV data.

model is superior to those of PIV experiments. Therefore, in order to discuss the results with considering the issues in resolution, averaging of PIV results in measurement planes and turbulence model predictions in calculated planes were

performed. The averaged data corresponds to the shaded region on the sketch shown in Fig. 7. In Fig. 7 the average of these three velocity magnitudes for each turbulence model are compared to the averages of PIV data. The results of

the all three turbulence models show very close trends with experimental data, and their predictions are almost equal to those of PIV results. Particularly considering the resolution of PIV experiments, the predictions of all three models are considered to be accurate. The standard k-ε model predicts slightly larger velocity magnitudes compared to the predictions of other turbulence models.

Further comparisons of turbulence models are based upon the jet angle characteristics. Two types of jet angles: slice jet angle and overall jet angle are calculated and compared in **Table 3**. The overall jet angle, or simply the jet angle, is the average angle of the all velocity data on nozzle exit plane for x and y components of the velocity and was calculated by the weighted average method. The slice jet angle is defined as the simple arithmetic mean of the velocity components on a specific plane.<sup>15)</sup> Table 3 indicates that standard k-ε and k-ω SST models predictions are very close to those of PIV measurements, realizable k-ε model on the other hand, predicts slightly higher velocity values.

For the final comparison **Fig. 8** is constructed, where both the velocity magnitudes along jet and the meniscus velocity predictions at single point 20 mm below the meniscus for three different turbulence models along with the Large Eddy Simulation (LES) model predictions and experimental measurements are demonstrated. LES is capable of capturing the

large scale eddies only and it is preferred in the applications where the velocity magnitudes are relatively smaller.<sup>15)</sup> The study which supplies the experimental data,<sup>15)</sup> provides the time history of the PIV and LES data, therefore in order to compare them with the predictions of the three turbulence model, the mean of the LES and PIV results are also calculated and shown in **Fig. 8(b)**. Figures 8(a) and 8(b) demonstrate that the predictions by three turbulence models are reasonable compared to the experimental data and averaged LES simulation results. Considering the speed of jet along its direction, the turbulence models predict close values to those PIV measurements, however LES model prediction is more consistent compared to the model predictions of the present study in terms of capturing the jet velocity trend of the PIV results. The predictions of the k-ε realizable model are closer to the LES predictions. Considering the meniscus velocity predictions shown in **Fig. 8(b)**, the standard k-ε model result is almost equal to the mean of the PIV measurements. The k-ω SST model also predicts close values to those of the PIV measurements.

Carrying on the study to determine the effects of flow rate controllers on mold flow, one turbulence model was chosen based on the aforementioned comparisons. The overall conclusions of previous comparisons lead us to accept standard k-ε and k-ω SST model predictions as accurate. In addition, the fast and easy converging behavior of the standard k-ε model during solutions made this model to be used in further calculations.

**Table 3.** Jet angle comparison.

		Experimental Results <sup>15)</sup>	k-ε Standard	k-ε Realizable	k-ω SST
Jet Angle		29°	31.02°	34.35°	31.80°
Slice Jet Angle	Center Plane	40.30° down	40.33° down	42.50° down	40.30° down
	12 mm Plane	22.80° up	21.48° up	23.36° up	21.14° up

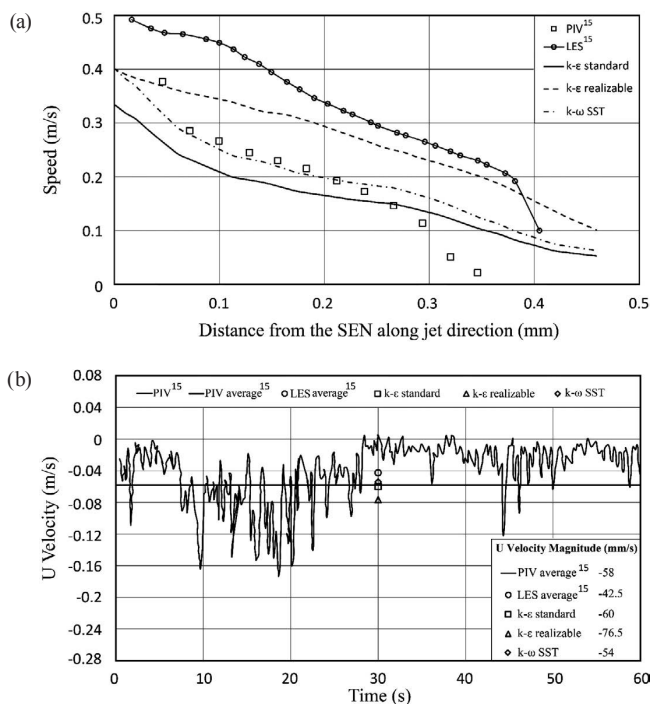


**Fig. 8.** Performance evaluation of three turbulence models with PIV data and LES simulations by (a) speed of jet along its direction, (b) u velocity values at meniscus region.

**5. Influence of Flow Controller**

There are two common flow controller techniques to regulate the flow from the tundish to the mold. In order to observe the effect of flow controller on mold flow structure, slide-gate and stopper rod controlled geometries were simulated under same throughput condition. Different controller openings were also simulated in order to quantify the effect of opening fraction on the mold flow. Five different slide-gate opening fractions were simulated. There are two most common approaches to determine the opening fraction of the slide-gate.<sup>3)</sup> Area fraction  $f_A$ , is the ratio of the overlapping area to nozzle bore area, whereas linear fraction  $f_L$ , is the ratio of the throttling plate to the bore diameter of the nozzle.<sup>3)</sup> The area and linear fraction openings,  $f_A$ ,  $f_L$ , of slide-gates simulations are tabulated in **Table 4**. In addition, simulations of different stopper rod openings were also performed to ultimately compare the performances of different flow rate control mechanisms on the mold flow structure. The stopper rod openings are tabulated in **Table 5**. The distance L is defined as the vertical distance from the tip of the stopper rod to the top of the UTN surface, and the distance R is the smallest distance from the lower UTN corner to the stopper rod bore. Opening percentage levels of stopper rod were also calculated by dividing the area of the cross section from where distance

**Table 4.** Slide-gate opening parameters.

Case Number	Case 1	Case 2	Case 3	Case 4	Case 5
Area Fraction	30%	40%	50%	60%	70%
Linear Fraction	41%	52%	60%	68%	76%

R is defined to the nozzle bore area.

### 5.1. Slide-Gate Controller

For the slide-gate controlled domain five different opening fractions were simulated. As discussed earlier, ladle changes result in liquid steel level changes in tundishes and the flow rate controller opening is increased to reduce the pressure drop across the opening, if constant throughout operation so called steady state casting is desired. The particular interest here is to investigate the opening effect on meniscus region under the constant throughput casting operation. The simulated area opening fractions of the slide-gates systems range from 30% to 70% in the present study.

The normalized velocity vectors on center plane of narrow face parallel to the broad face of the mold for three sample cases are demonstrated in Fig. 9(a). The aforementioned approaches, used for constructing Fig. 4, were adopted for Fig. 9. Figure 9(a) shows that the formation of double roll flow pattern is evident in all three cases. Quali-

**Table 5.** Stopper rod opening parameters.

Case Number	Case 1	Case 2	Case 3	Case 4	Case 5
Distance L (mm)	31 mm	29 mm	27 mm	25 mm	23 mm
Distance R (mm)	1.94 mm	2.88 mm	4 mm	5.27 mm	6.66 mm
Area Fraction	35%	46%	57%	69%	81%

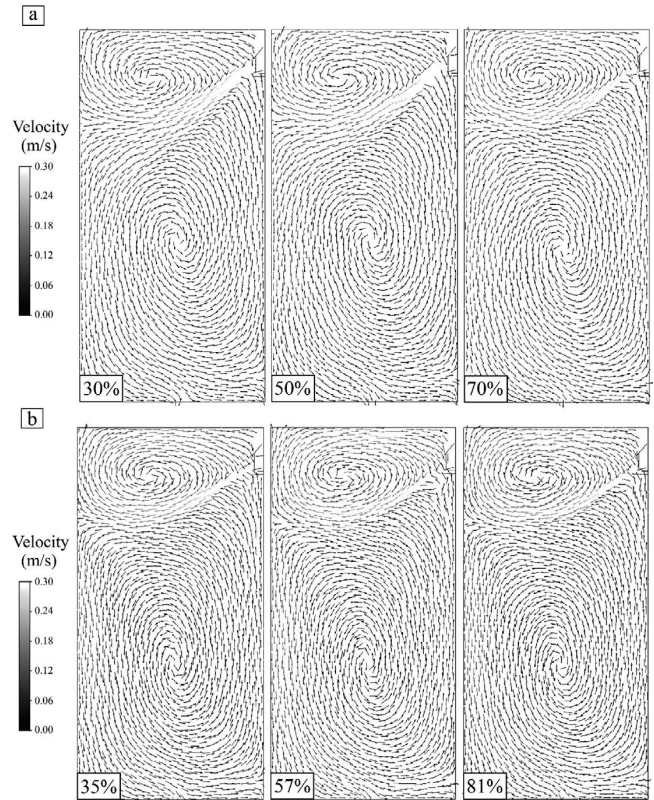


**Fig. 9.** Normalized velocity vectors at the center plane of the mold for (a) three different slide-gate openings, (b) three different stopper rod openings.

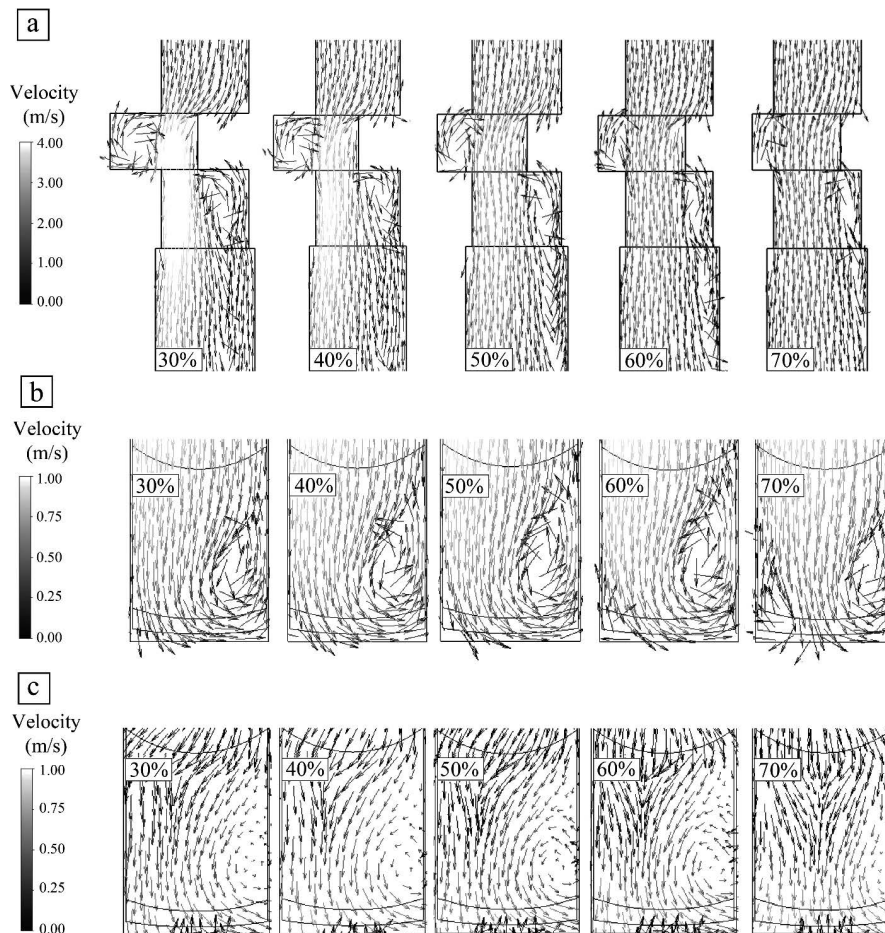


**Fig. 10.** Velocity vectors (a) at slide gate region on the symmetry plane, (b) at nozzle region on the symmetry plane, (c) at nozzle region on the port exit plane.

tatively, similar flow patterns are observed.

Further comparison of the results for different cases is shown in Fig. 10, where velocity fields in the SEN are presented. Figure 10(a) demonstrates the velocity vectors at slide-gate region on symmetry plane whereas Figs. 10(b) and 10(c) illustrate the velocity vectors at port region on the symmetry plane and on the port exit plane, respectively. The velocity scale for each one is shown on the left side of the corresponding image.

As shown in Fig. 10(a) the recirculation zones around the slide-gate sections of the SEN get smaller with the increasing opening fractions. Figures 10(b) and 10(c) show that the one-sided recirculation zones within the port exist for all of the five slide-gate openings. Figure 10(c) illustrates similar results to Fig. 10(a), since it demonstrates the adverse relation between the slide-gate opening fraction and the

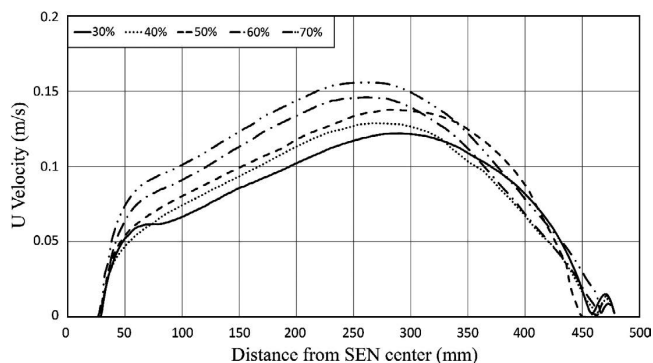


Fig. 11. Meniscus velocities at the center plane of the mold for five different slide gate openings.

recirculation zones.

The velocity magnitudes at meniscus region are plotted for five different slide-gate openings are shown in Fig. 11. Data line is generated at meniscus on centerline of narrow face of the mold. The velocity magnitudes show that as the slide-gate opening increases, the meniscus velocities also increase. Up to 30% increase in meniscus velocities can be achieved at constant throughput just altering the slide-gate opening. It is also important to mention that the maximum velocity point moves toward SEN as the gate opening increases.

### 5.2. Stopper Rod Controller

Similar to slide-gate controlled domain, five different opening fractions were simulated under the same throughput conditions, for stopper rod controlled domain. The opening distances of stopper rod simulations are tabulated in Table 5. The simulated opening fractions of the stopper rods range from 35% to 81%. The normalized velocity vectors on central plane of the mold parallel to broad face for three sample stopper rod openings are illustrated in Fig. 9(b). Figure 9(b) shows that the formation of double roll flow pattern is evident in all five cases. Both qualitatively and quantitatively very similar flow patterns are obtained.

The effect of stopper rod on flow fields within the SEN and inlet of the UTN is illustrated in Fig. 12. Figure 12(a) shows the velocity vectors at stopper rod inlet on symmetry plane where Figs. 12(b) and 12(c) illustrate the velocity vectors at port region on the symmetry plane and on the port exit plane, respectively. The velocity scale for each one is shown on the left side of the corresponding image. Figure

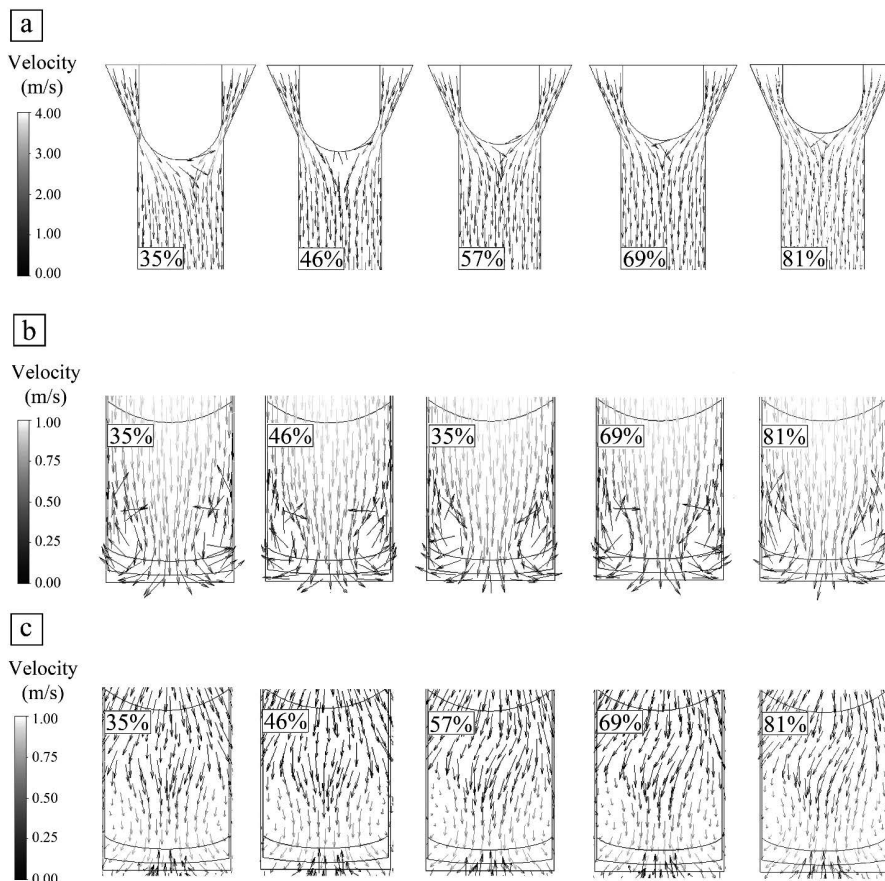


Fig. 12. Velocity vectors (a) at stopper rod region on the symmetry plane, (b) at nozzle region on the symmetry plane, (c) at nozzle region on the port exit plane.

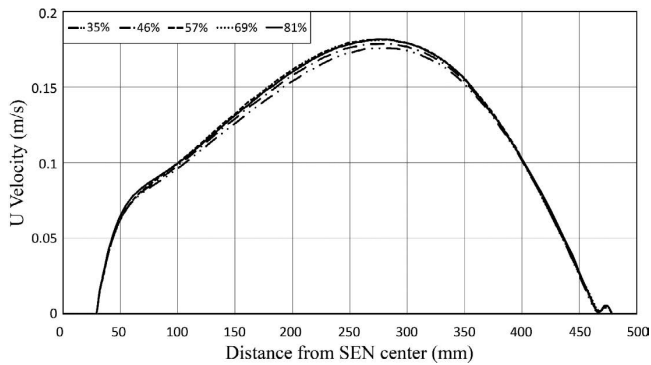


Fig. 13. Meniscus velocities at the center plane of the mold for five different stopper rod openings.

12(a) illustrates very similar flow fields around UTN inlet. Figures 12(b) and 12(c) show that the two-sided recirculation zones within the port exist for all of the five stopper rod cases. At this point there is great difference between slide-gate and stopper rod controllers, since stopper rods produce two-sided almost symmetrical weak recirculation zones whereas, slide-gate controllers produce one sided very strong recirculation zones at the bottom of the port as indicated in Figs. 10 and 12.

The velocity magnitudes at meniscus region are plotted for five different stopper rod openings and demonstrated in Fig. 13. Data line is generated at meniscus on centerline of narrow face of the mold. Figure 13 demonstrates no significant difference between the meniscus velocities indicating that meniscus velocities are not affected by the changes in the stopper rod opening fraction.

## 6. Conclusions

Ladle change operations in continuous casting machines result in liquid steel level changes in tundishes. During this transient event of production, the flow rate controller opening is increased to reduce the pressure drop across the opening, which helps to keep the mass flow rate constant for the reduced liquid steel level in tundish, if constant throughout operation so called steady state casting is desired. Therefore, the effects of different opening levels for flow controllers on mold flow structure need to be understood.

The present study aims to investigate the effect of different flow controllers on mold flow structure using CFD modeling. In addition, the effect of flow controller opening on meniscus flow is quantified. A CFD model was developed for a water model, which had 0.4-scale geometry of the nozzle and the mold of an actual caster for steady state operation. For the constructed simulation domain a mesh independency study was performed. The results demonstrate that the mesh independent solution was reached with the mesh which do not alter the velocity predictions more than 1%. The resulting mesh contains both tetrahedral and prismatic elements and consists of approximately 1 million nodes and 4 million elements.

The performances of three different turbulence models, standard  $k-\epsilon$ , realizable  $k-\epsilon$  and  $k-\omega$  SST, were compared and validated against PIV data available in literature. Despite all three models displayed good performances, one

was selected due to its fast and easy converging performance. The standard  $k-\epsilon$  model was used for the rest of the study to quantify the effect of different flow controllers and their opening levels on mold flow structure.

Five different opening fractions for both slide-gate and stopper rod flow controllers were simulated for constant throughput condition. The results indicate that the flow structure within the mold, particularly meniscus region, is influenced by the alterations in the slide-gate opening. The main mechanism behind this alterations is the one-sided recirculation zones within the slide-gate section. These alterations are important since they ultimately affect the quality of the steel produced. Thus, during transient events such as ladle changes, if constant throughout operation so called steady state casting is desired, adjusting the slide-gate opening to obtain constant throughput alters the flow structure in the mold. Therefore, considering the fact that the majority of the quality problems occur in the meniscus region, in order to produce the same quality steel in continuous casting process during transient events, abandoning the common practice of keeping constant throughput may be useful. This claim is supported by the fact that stable meniscus flow can be achieved by altering the flow rate, which in turn might results in same quality steel. On the other hand, for a stopper rod controlled system, the flow structure and velocities in the meniscus region are not affected by the changes in the opening fraction of the controller indicating that, despite the level changes in the tundish, stopper rods can provide same mold flow structures under same throughput condition.

## Acknowledgments

This study was financially supported by Middle East Technical University (METU) BAP (Scientific Research Projects) Coordination.

## REFERENCES

- 1) B. G. Thomas: The Encyclopedia of Materials: Science and Technology, Vol. 2, Elsevier Science, Oxford, UK, (2000), 41.
- 2) E. S. Szekeres: Brimacombe Continuous Casting Course Proc., Vol. 1, Brimacombe Continuous Casting Society, Vancouver, BC, (2007), A1.
- 3) B. G. Thomas: Making, Shaping and Treating of Steel, Vol. 5 (Chapter 14), AISE Steel Foundation, Pittsburgh, PA, (2003), 1.
- 4) H. Bai and B. G. Thomas: *Metall. Mater. Trans. B*, **32** (2001), 253.
- 5) H. Bai and B. G. Thomas: *Metall. Mater. Trans. B*, **32** (2001), 707.
- 6) V. A. Kononov, V. P. Vasilenko and A. A. Alpatov: *Refract. Indust. Ceram.*, **54** (2014), 6.
- 7) R. Chaudhary, G. G. Lee, B. G. Thomas, S. M. Cho, S. H. Kim and O. D. Kwon: *Metall. Mater. Trans. B*, **42** (2011), 300.
- 8) R. Liu, J. Sengupta, D. Crosbie, M. M. Yavuz and B. G. Thomas: AISTech Proc., AIST, Warrendale, PA, (2011), 1619.
- 9) H. A. A. Lima and M. G. Rogana: AISTech Proc., AIST, Warrendale, PA, (2011), 473.
- 10) R. Liu, B. G. Thomas, J. Sengupta, D. S. Chung and M. Trinh: *ISIJ Int.*, **54** (2014), 2314.
- 11) L. J. Heaslip and J. Schade: *Iron Steelmaker*, **26** (1999), 33.
- 12) L. J. Heaslip, I. D. Sommerville, A. McLean, L. Swartz and W. G. Wilson: *Iron Steelmaker*, **14** (1987), 49.
- 13) B. G. Thomas and H. Bai: Material Processing in the Computer Age, Vol. 3, ed. by V. Voller and H. Henein, TMS, Warrendale, PA, (2000), 279.
- 14) J. Westerweel: *Meas. Sci. Technol.*, **8** (1999), 1379.
- 15) B. G. Thomas, H. Bai, S. Sivaramakrishnan and S. P. Vanka: Int. Symp. on Cutting Edge of Computer Simulation of Solidification and Processes, ISIJ, Tokyo, (1999), 113.
- 16) ANSYS Inc.: ANSYS User's Guide Documentation, Solver Theory, version 13, ANSYS Inc., Canonsburg, PA, (2013), 578.